Journal of Materials Chemistry A

Optical properties of Ytterbium-doped and undoped $Cs_2AgInCl_6$ thin films deposited by co-evaporation of chloride salts

Journal:	*Journal of Materials Chemistry A*
Manuscript ID	TA-ART-07-2023-004335.R1
Article Type:	Paper
Date Submitted by the Author:	30-Aug-2023
Complete List of Authors:	Liu, Yukun; New York University, Department of Chemical and Biomolecular Engineering Jain, Pulkita; New York University Tandon School of Engineering, Department of Chemical and Biomolecular Engineering Cleveland, Iver; New York University Tandon School of Engineering, Chemical and Biomolecaulr Engineering Tran, Minh; New York University Tandon School of Engineering, Chemical and Biomolecaulr Engineering Department Sarp, Seda; New York University Tandon School of Engineering, Department of Chemical and Biomolecular Engineering Sandrakumar, Kajini; New York University Tandon School of Engineering, Department of Chemical and Biomolecular Engineering Rodriguez, Rafa; New York University Tandon School of Engineering, Department of Chemical and Biomolecular Engineering Aydil, Eray; New York University Tandon School of Engineering, Department of Chemical Engineering and Biomolecular Engineering

ARTICLE

Optical properties of Ytterbium-doped and undoped $Cs_2AgInCl_6$ thin films deposited by co-evaporation of chloride salts

Received 00th January 20xx,
Accepted 00th January 20xx

DOI: 10.1039/x0xx00000x

Yukun Liu,[a] Pulkita Jain,[a] Iver J. Cleveland,[a] Minh Tran,[a] Seda Sarp,[a] Kajini Sandrakumar,[a] Rafa Saa Rodriguez[a] and Eray S. Aydil*[a]

The double halide perovskite $Cs_2AgInCl_6$, first synthesized in 2017, is a potential lead-free alternative to $CsPbCl_3$ for optoelectronic applications, but its discovery is recent, there are knowledge gaps and controversies in its optical properties, and its formation as a thin film for practical use remains difficult due to the poor solubility of the precursors used in solution synthesis. Herein, we report the formation of $Cs_2AgInCl_6$ thin films through reactive physical vapor deposition (PVD) via co-evaporation of CsCl, AgCl, and $InCl_3$ for the first time in a solvent-, ligand- and oxygen-free environment. We also doped these films with Yb^{3+} by co-evaporating $YbCl_3$. Consistent with previous reports, the undoped films emit orange luminescence peaking at 630 nm, while Yb-doped films emit near-infrared (NIR) luminescence at 990 nm. Using the excitation spectrum of the orange and NIR emissions from the Yb^{3+} dopant and absorbance spectra, we determine the $Cs_2AgInCl_6$ band gap to be 3 eV. Up to 12% (of Ag or In lattice positions) Yb could be incorporated into the film without disrupting its cubic crystal structure or stability. The highest NIR photoluminescence quantum yield was 20%, achieved in films doped with 8% Yb. We show that the emission at 630 nm, previously assigned to self-trapped excitons in $Cs_2AgInCl_6$ persists, shifted only slightly (10s of nm), in $Cs_2AgBiCl_6$, $Cs_2AgBiBr_6$, and $Cs_2NaBiCl_6$, double perovskites with significantly different band gaps, suggesting that at least some of this emission intensity is due to a common defect, possibly In and Bi antisite defects, and not necessarily only due to self-trapped excitons.

Introduction and a Brief Literature Review

The double perovskite, $Cs_2AgInCl_6$, first synthesized by Volonakis *et al.*[1], is a lead-free alternative to halide perovskites such as $CsPbCl_3$ for optoelectronic applications.[2] $Cs_2AgInCl_6$ has been reported to have prolonged light, moisture, and air stability,[3–6] and to retain its cubic crystal structure ($Fm\bar{3}m$) at up to 500 °C.[7,8] Its tolerance factor and octahedral factor are within the stable region,[1,9] and theoretical studies have predicted the compound to be thermodynamically stable.[10,11]

Synthesis

Volonakis *et al.* first made this white powder compound via precipitation.[1] Shortly after Volonakis, Zhou *et al.*[5] and Luo *et al.*[8] grew single crystals hydrothermally and explored their optical properties. In an alternative approach, Locardi *et al.* reported the first colloidal synthesis of cubic $Cs_2AgInCl_6$ nanocrystals in an organic solvent from metal carboxylate precursors using oleic acid and oleylamine ligands to keep the nanocrystals dispersed and to gain control over the nanocrystal size distribution.[7] The poor solubility of the precursors in solution methods remains a disadvantage that may limit the fabrication of $Cs_2AgInCl_6$ thin films and applications in devices. Consequently, dry methods such as the conventional high-temperature (400°C) solid-state vacuum synthesis of $Cs_2AgInCl_6$ fine powder have also been reported,[12] though forming thin films from these powders is not convenient and requires additional processing. Solvent-free and ligand-free vapor deposition by co-evaporation of CsCl, AgCl, and $InCl_3$ has not yet been reported to form $Cs_2AgInCl_6$ and is one of the goals of this study.

Optical Properties

The optical properties and band gap of $Cs_2AgInCl_6$ immediately became a topic of debate with its first synthesis. Volonakis *et al.* saw a clear absorption onset at 3.3 eV and reported this value as the material's band gap, consistent with the white appearance of the powders.[1] However, Volonakis *et al.* also noticed an absorption feature at 2.1 eV (590 nm) and the compound turning orange under photoexcitation. Based on these observations, they attributed the 2.1 eV feature to defects, possibly photoinduced. This absorption feature was also accompanied by photoluminescence (PL) at ~608 nm, presumed to originate from the same levels. Their Density-functional-theory (DFT) calculations predicted a direct band gap ranging from 2.1 eV (DFT with HSE06 functional) to 3.3 eV (DFT with PBE0) depending on the structure relaxation method and functional used. In the same year Volonakis' article appeared, Meng *et al.*[13] suggested an alternative explanation for the 2.1 eV absorption feature and PL from $Cs_2AgInCl_6$. Specifically, Meng *et al.*[13] showed that double perovskites of the type

[a] *Department of Chemical and Biomolecular Engineering, New York University, Tandon School of Engineering, Brooklyn, New York 11201 USA.*

†Electronic Supplementary Information (ESI) available: [details of any supplementary information available should be included here]. See DOI: 10.1039/x0xx00000x

$A_2B^+B^{3+}X_6$ can exhibit inversion-symmetry-induced parity forbidden or weak transitions between band edges and proposed that perhaps the weak feature was due to such a transition at the Γ point and not due to a defect. This proposed dark transition was also examined experimentally in high-quality $Cs_2AgInCl_6$ single crystals with low trap density (8.6 ±1.9 × 10^8 cm^{-3} as determined from space charge limited current measurements) by Luo *et al.*,[8] who found a sharp absorption edge rising at 3.2 eV and an extremely weak absorption at 2.1 eV accompanied by PL also at 2.1 eV with a lifetime of 566.9 ns. Based on the long lifetime, Luo *et al.* argued that the origin of the weak absorption and PL is due to a parity-forbidden band-to-band transition, as proposed by Meng *et al.*. However, long emission lifetimes are not necessarily proof for band-to-band parity forbidden transitions because defects and defect-bound excitons, substitutional impurities may also have long lifetimes. Indeed, Zhou *et al.*,[5] also working with single crystals, observed the sharp absorption onset at 3.23 eV and PL at 2.1 eV but assigned the latter to a defect because the emission intensity saturated with excitation power density, arguing that such saturation is not expected from band-to-band transitions.[5] Zhou *et al.* reported a PL decay time of 100 μs, more than two orders of magnitude slower than that measured by Luo *et al.*

The DFT calculations by Meng *et al.* employed generalized gradient approximation (GGA) with Perdew-Burke-Ernzerh (PBE) and HSE06 functionals and predicted parity-forbidden direct band gap transitions of 1.03 and 2.38 eV, respectively. The close agreement between the predicted 2.38 eV gap and the 2.1 eV PL with weak absorption near the same energy appeared to fit the interpretation that the transition across the direct gap at the Γ point is parity forbidden, and the PL is band-to-band transition. However, Luo *et al.* changed their interpretation after conducting DFT calculations using the GW approximation and finding the band gap to be 3.27 eV, much closer to the experimentally measured value but still parity-forbidden.[2] They assigned the emission at 2.1 eV PL to emission from a self-trapped exciton (STE) to explain the huge shift from the bandgap energy of $\boldsymbol{E_g} = 3.27$ eV. STEs are excitons trapped by a lattice distortion, such as the Jahn-Teller distortion of the $AgCl_6$ octahedron, as suggested by Luo *et al.*.[2] When they recombine radiatively from their trap state, the emission energy is given by $\boldsymbol{E_{PL} = E_g - E_b - E_d - E_{st}}$, where $\boldsymbol{E_b}$, $\boldsymbol{E_d}$, and $\boldsymbol{E_{st}}$ are the exciton binding energy, lattice-distortion energy, and exciton self-trapping energy, respectively. Luo *et al.* calculated the $\boldsymbol{E_{PL}}$ value to be 1.82 eV close to the location of the observed PL,[2] and assigned this emission to STEs.

Most measured band gap values cluster around 3.3 eV, but a few somewhat higher values measured by diffuse reflectance have also been reported by Tran *et al.*[4] (3.53 eV) and Zhao *et al.*[12] (3.55 eV). Locardi *et al.* found an even higher bandgap, 4.38 eV, for $Cs_2AgInCl_6$ nanocrystals dispersed in hexane and attributed it to quantum confinement.[7]

Doping for Visible and Near Infrared Emission

To date, the main interest in $Cs_2AgInCl_6$ has been for lighting applications, and to that end, efforts have concentrated on increasing the efficiency of the broadband warm white emission at ~600 nm. Various metals, including Na^+, Bi^{3+}, Cr^{3+}, Cu^{2+}, and Mn^{2+} ions, were alloyed or doped into the lattice to engineer the material's optical properties by breaking the parity forbidden band gap transition or tuning the material band bap.[2,3,6,12,14–17] Visible warm-white PLQY,s as high as 87%, have been achieved by replacing 30-40% of the Ag with Na and a small amount of In (0.04%) with Bi,[2,15] though similar compositions in nanocrystals resulted in lower, 22-37%, PLQY. PLQY was sensitive to surface ligands and post-synthesis treatments, which was interpreted as sensitivity to the surface defects in nanocrystals.[18] Indeed, Han *et al.* measured the PLQY across a wide range of crystal sizes, from nm to mm, in $Cs_2AgBi_{0.125}In_{0.875}Cl_6$ and showed that the PLQY declined with decreasing crystal size attributed to the formation of nonradiative defects.[3]

Ytterbium-doped $Cs_2AgInCl_6$ was also investigated as a lead-free halide perovskite host for NIR emission, though PLQY without any co-dopants has been low (3-4%).[19,20,21,22] One difficulty is Yb incorporation into micro and nanocrystals in wet and colloidal synthesis methods.[21] For instance, Mahor *et al.* could incorporate only 0.1 to 1.6% Yb into $Cs_2AgInCl_6$ microcrystals and 6.2% of Yb into thin films even though the precursor solutions contained up to 50% Yb.[22] Co-doping $Cs_2AgInCl_6$ with Sb^{3+} and Yb^{3+} in solution synthesis enhanced the NIR PLQY as high as 50%.[23] A similar enhancement up to 45% PLQY was achieved by substituting Cr^{3+} instead of Sb^{3+} in $Cs_2AgInCl_6$ microcrystals synthesized via hydrothermal synthesis. [24] Co-doping with Bi^{3+} and Yb^{3+} also showed more intense NIR emission than doping with Yb^{3+} alone, but no PLQY value was reported.[25] Other reported Yb^{3+} co-dopants included Er^{3+} for up-conversion, [26] and a cocktail of Nd/Yb/Er/Tm/Bi in $Cs_2AgInCl_6$ microcrystals for vis-NIR ultra-broadband (400 to 2000 nm) emission with a high PLQY of 40%.[27]

This Article

This article focuses on undoped and Yb-doped $Cs_2AgInCl_6$ polycrystalline thin films prepared by CsCl, AgCl, $InCl_3$, and $YbCl_3$ co-evaporation and their subsequent condensation and reaction on glass substrates. In this form of reactive physical vapor deposition (PVD), the precursors are co-evaporated onto the substrate surface in a high vacuum, condensing and reacting to form the double perovskite. Complete reaction and grain growth are achieved by post-annealing. PVD provides oxygen-, ligand- and solvent-free synthetic method with facile Yb incorporation and the ability to scale up to large areas. We achieved 20% NIR PLQY from Yb-doped films, the highest achieved without co-doping. We clarify an apparent discrepancy in the interpretation of the orange-red emission. Like others, we observe the emission around ~ 2 eV (≈ 620-640 nm) in $Cs_2AgInCl_6$, but this emission also persists, shifted only slightly (10s of nm), in $Cs_2AgBiCl_6$, $Cs_2AgBiBr_6$, and $Cs_2NaBiBr_6$, double perovskites with significantly different band gaps, suggesting strongly that the emission is due to a defect with a similar structure common to these materials.

Experimental Methods

Thin Film Synthesis

The $Cs_2AgInCl_6$ thin films doped with or without Yb were deposited using a high vacuum six-source physical vapor deposition (PVD) system (Angstrom Engineering) with a base pressure of approximately 10^{-8} torr.[28] The PVD chamber is enclosed in a nitrogen-filled glovebox, allowing all precursors to be loaded into the PVD system's evaporation crucibles without exposure to the atmosphere. Films were deposited on glass substrates secured on a rotating stage (10 rpm). A movable combinatorial deposition mask allowed the deposition on sixteen 10 × 10 mm^2 substrates (4 × 4 matrix of substrates) and the formation of four identical films with four different (or same) compositions or the deposition on three 25 × 75 mm^2 substrates with different (or same) compositions. Before deposition, the substrates were cleaned by first ultrasonication (Branson 3800) for 30 minutes in a 50/50 vol% acetone (ACS grade, VWR) and isopropanol (99.5%, VWR) solution, followed by drying in an oven and plasma-cleaning for 30 min in an oxygen plasma cleaner (Harrick Plasma PDC-001-HP). A circulating chiller system (ºLAUDA) controlled the substrate stage temperature, and substrates were maintained at 30 °C during depositions. The evaporation rates of each precursor were monitored via individual quartz crystal microbalances (QCMs) with a tooling factor of 39.7 used for CsCl, AgCl, $InCl_3$, and $YbCl_3$. Precursors were loaded in alumina ampoules and placed in crucible heaters for evaporation. CsCl (99.999%, Alfa Aesar), AgCl (99.995%, Beantown Chemical), and $YbCl_3$ (hydrate, 99.9%, REacton™) were baked overnight at 100 °C, 100 °C and 110 °C respectively. $InCl_3$ (99.999%, Sigma-Aldrich) was kept overnight in a vacuum at room temperature before use. Precursors, CsCl, AgCl, and $InCl_3$, were evaporated in the molar stoichiometric ratios (2:1:1) of the target $Cs_2AgInCl_6$ compound, and Yb doping was varied between 0-0.12 (*i.e.,* 0-12% equivalent of Ag or In lattice positions). Specifically, the evaporation rates of CsCl, AgCl, and $InCl_3$ were 1.32 Å/s, 0.40 Å/s, 1 Å/s, and $YbCl_3$ were 0.02, 0.04, 0.06, 0.09, 0.11, and 0.13 Å/s respectively. The evaporation source temperatures were manipulated to keep the evaporation rates constant and were approximately 590 °C, 630 °C, 250 °C, and 670 °C, respectively. The chamber pressure during the deposition was approximately 10^{-7} torr. The deposited films were either characterized as deposited or after annealing in the glovebox or the air.

We have also deposited $Cs_2NaBiCl_6$, $Cs_2AgBiCl_6$, and $Cs_2AgBiBr_6$, in addition to $Cs_2AgInCl_6$, for comparing their PL. Methods for depositing $Cs_2AgBiBr_6$ were described previously.[29,30] To deposit $Cs_2NaBiCl_6$, the three precursors, CsCl (99.9%, Sigma-Aldrich), NaCl (99.99%, Sigma-Aldrich), and $BiCl_3$ (99.9%, Alfa Aesar), were loaded into separate crucibles and baked under vacuum overnight at 110 °C, 500 °C and 60°C respectively. The films were deposited by co-evaporating all precursors onto glass substrates (25 x 75 mm^2) while maintaining the substrate temperatures at 30°C throughout the deposition. The specific film used in this study was annealed in a nitrogen-filled glovebox at 250 °C for one hour. $Cs_2AgBiCl_6$ was deposited, in a similar manner to $Cs_2AgInCl_6$, by co-evaporating $BiCl_3$ (99.997%, Thermo Scientific), CsCl (99.999%, Alfa Aeser) and AgCl (99.995%, Beantown Chemical) onto 10 × 10 mm^2 glass substrates maintained at 30 °C. Before evaporation, $BiCl_3$ was baked overnight under vacuum at 60 ℃, while AgCl and CsCl were baked at 100 ℃. The evaporation fluxes were maintained ($BiCl_3$ (0.85 Å/s), AgCl (0.33 Å/s), and CsCl (1.1 Å/s) to obtain stoichiometric $Cs_2AgBiCl_6$ and the deposition lasted for 30 minutes. The film reported in this study was annealed at 300 ℃ for 1 hour inside the nitrogen-filled glove box.

All films were characterized under ambient conditions. X-ray diffraction patterns (XRD) were collected using a Bruker AXS D8 DISCOVER GADDS Micro-diffractometer equipped with a VÅNTEC-2000 area detector and a Cu source ($\lambda_{Cu-K\alpha}$=1.54178 Å) operated at 40 kV and 40 mA. The scans were area averaged by oscillating the sample laterally with scan oscillation amplitudes across an area of 2 × 2 mm^2. High-resolution images of film topography were recorded in a MERLIN Carl Zeiss field emission scanning electron microscope at 5 kV acceleration voltage and 110 pA beam current under an in-lens (annular secondary electron) detector and an SE2 (Everhart-Thornley type) detector. Film elemental compositions were determined using energy dispersive X-ray spectroscopy (EDS) at 15 kV acceleration voltage and 2000 pA beam current. The EDS measurements collected over 1 µm × 1 µm areas at different locations were averaged and reported. Film optical absorption between 300-2000 nm was measured in a UV-Vis-NIR Spectrophotometer (Agilent Technologies Cary 5000) with a bare glass substrate as the reference. As described previously,[31–33] film thicknesses were determined from the precursor deposition rates or by fitting the thin-film interference fringes in the optical transmission measurements to an optical model of a thin film on a thick, finite, non-absorbing substrate.[31,33] Film thicknesses of select films were also determined from cross-sectional Scanning Electron Microscope images (Fig. S1) to check the thickness from thin film interference. All methods agreed within experimental error. Typical film thicknesses were between 400-600 nm, and films adhered well to the substrate. Steady-state photoluminescence (PL) was measured in a HORIBA spectrophotometer (QM-8075-21-C), with an Xe-arc lamp (75W, LPS 100) as the light source. Near-infrared PL was excited at 370 nm (5 nm bandwidth, filtered by a double monochromator) and was detected after being filtered with a single monochromator by an InGaAs detector (DSS-IGA020L/100KHZ) cooled by liquid nitrogen. A red-extended Hamamatsu PMT was used on the same monochromator to detect emissions from UV to NIR. NIR quantum yield (PLQY) was measured in an integrating sphere (HORIBA Quanta-ϕ). The lamp power at 370 nm and 990 nm was measured with a power meter (Newport 843-R) and a photodetector (Newport 818-UV). Details of the PLQY calculations were reported previously.[32] Time-resolved photoluminescence (TRPL) was measured using time-correlated single photon counting (TCSPC). A pulsed diode

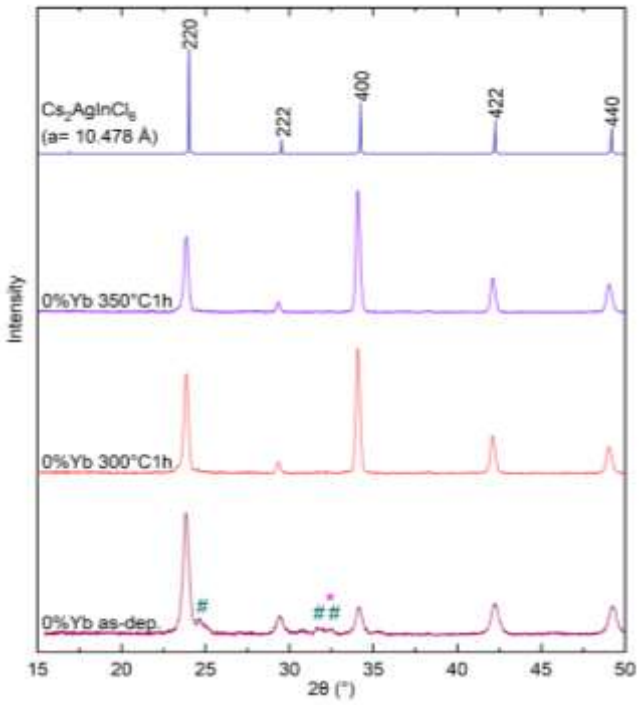

Fig. 1 XRD patterns, from bottom to top, of an undoped (0% Yb) film as-deposited, after annealing in a nitrogen-filled glovebox at 300 °C and at 350°C for one hour. All XRD measurements were taken at room temperature and under ambient conditions. Simulated XRD pattern of $Fm\bar{3}m$ cubic $Cs_2AgInCl_6$ with a = 10.478 Å is shown for comparison. Impurity and unreacted precursor XRD peaks are labeled with # for $Cs_2In_3Cl_9$ and with * for AgCl. The XRD are offset along the intensity axis for clarity.

laser at 375 nm (Horiba Delta Diode 375L) was used to produce narrow pulses (<50 ps) at 1 MHz, and PL was detected using the same red-enhanced PMT for steady-state measurements. The PMT limited the time resolution. PMT response was measured by scattering laser light from a glass substrate without the film, collecting photons to the same peak value, and then subtracting it from the TRPL data.

Results and Discussion

Undoped Films

Undoped $Cs_2AgInCl_6$ thin films were deposited and studied first to examine their optical properties without the Yb dopant. Fig. 1 shows the XRD patterns of the as-deposited film and the films annealed at 300 °C and 350 °C for one hour. Simulated (using VESTA)[34] XRD pattern of cubic ($Fm\bar{3}m$) $Cs_2AgInCl_6$ with lattice parameter[8] a = 10.478 Å is also shown in Fig. 1 for comparison. XRD from the (220), (222), (400), (422), and (440) planes of cubic $Cs_2AgInCl_6$ were detected from the as-deposited film with no further annealing, confirming its formation even at 30 °C. Thus, $Cs_2AgInCl_6$ is stable at room temperature, unlike $Cs_2AgInBr_6$, and forms immediately upon condensation of the precursors on the substrate.[31] However, weak impurity phase diffractions from the ternary layered perovskite, $Cs_3In_2Cl_9$, and unreacted AgCl are also detected ($Cs_3In_2Cl_9$ $2\theta_{(300)}$ = 24.22°, $2\theta_{(223)}$ = 31.73°, $2\theta_{(116)}$=32.64°; AgCl $2\theta_{(200)}$=32.26°). XRD pattern of the as-deposited film is compared to simulated XRD

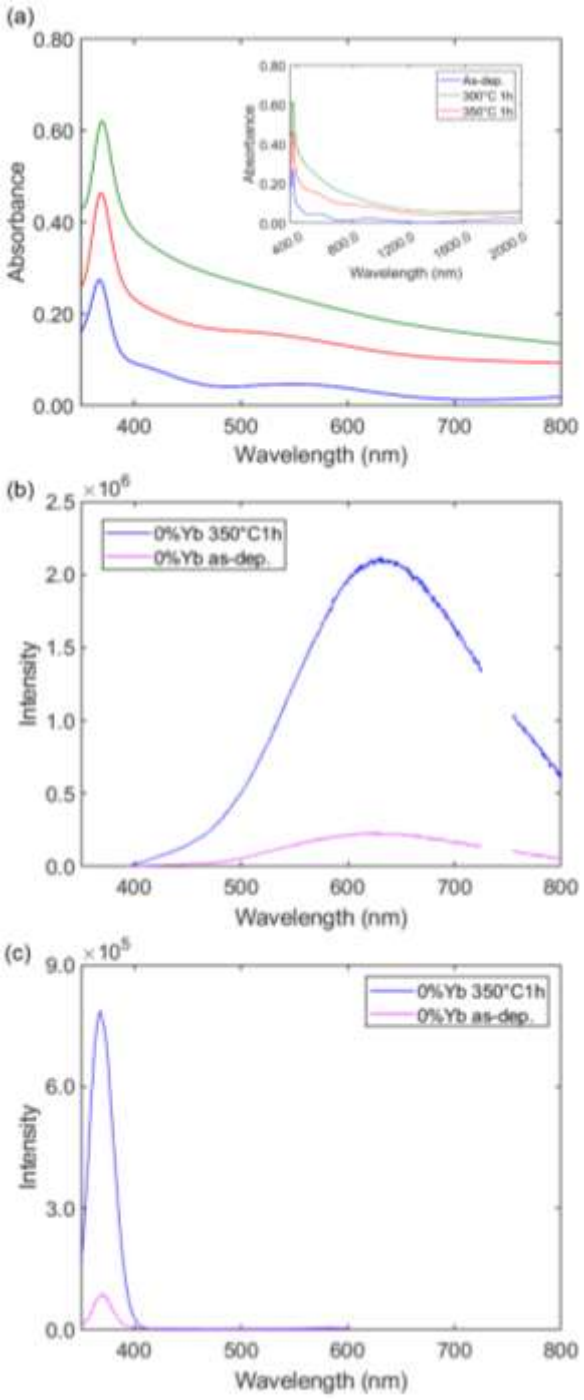

Fig. 2 (a) Absorbance (more strictly optical extinction) of an undoped as-deposited $Cs_2AgInCl_6$ film and after annealing in the nitrogen-filled glove box at 300 °C and 350 °C for one hour. Inset is the same over a wider range to show the thin film interference fringes. (b) Photoluminescence upon excitation at 370 nm from an undoped as-deposited $Cs_2AgInCl_6$ film and after annealing in the nitrogen-filled glove box at 350°C for one hour. (c) Excitation spectrum of the emission at 630 nm for the films in (b).

patterns of the possible impurity phase $Cs_3In_2Cl_9$, and the precursors, CsCl, AgCl, and $InCl_3$, in Supplementary Information Fig. S2. The impurity phase peaks disappeared once the as-deposited samples were annealed at 300 °C and 350 °C for one hour, and the remaining XRD peaks matched cubic $Cs_2AgInCl_6$. Unlike $Cs_2AgInBr_6$, the $Cs_2AgInCl_6$ polycrystalline crystal

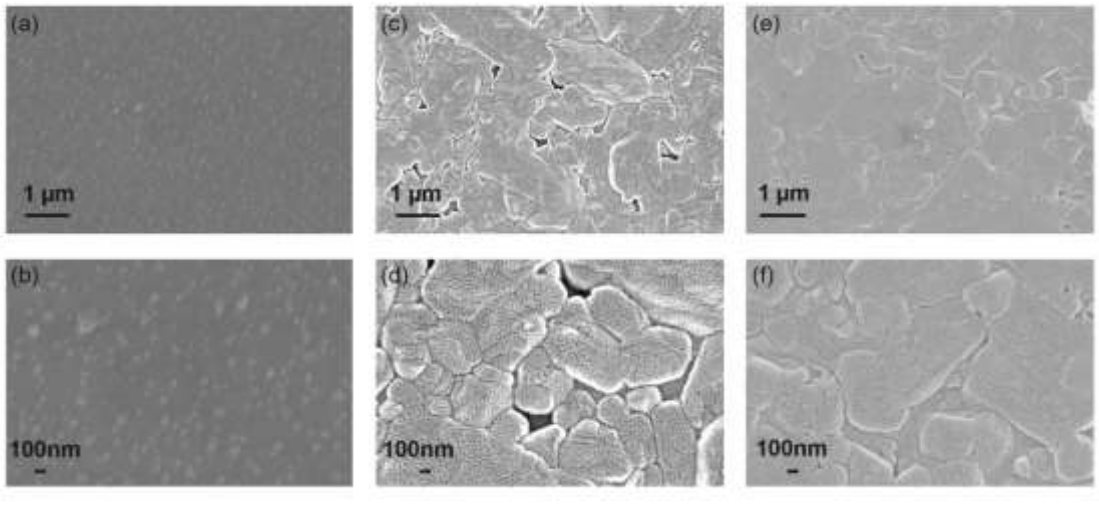

Fig. 3 SEM images of undoped $Cs_2AgInCl_6$ films (a, b) as deposited, annealed at (c, d) 300 °C and (e, f) 350 °C for one hour at two different magnifications.

structures are stable after annealing at 350 °C. The as-deposited film shows (220) texturing, which disappears upon annealing, and the grains grow to show clear (400) texturing, suggesting that the Cs-terminated (400) planes are the preferred thermodynamically low energy planes. Consistent with this, the EDS measurements gave slightly Cs-rich films. The elemental composition of the undoped film annealed at 300 °C for one hour was 25.5% Cs, 12.3% Ag, 8.6% In, and 53.2% Cl, close to the expected $Cs_2AgInCl_6$ composition (20% Cs, 10% Ag, 10% In, and 60% Cl) within the error of EDS.

Optical Properties of Undoped $Cs_2AgInCl_6$ Films

Fig. 2a shows the UV-Vis-NIR absorbance of the undoped as-deposited $Cs_2AgInCl_6$ films after annealing in the glove box for one hour at 300 °C or 350 °C. An absorption peak appears at 370 nm, and absorption rises at around 400 nm, but scattering obscures the onset of absorption. Strictly speaking, Fig. 2 shows the optical extinction because the data includes scattering and thin film interference fringes, clearly visible above ~500 nm in the data for the as-deposited film (Fig. 2 inset). Scattering and thin film interference obscures a clear absorption onset, expected around ~ 390-400 nm. Scattering is significant for annealed films. Crystal sizes grow after the films are annealed, which also explains the increased light scattering in Fig. 2a: as the grains grow to several 100s of nm, the film scatters light in the visible range of the electromagnetic spectrum. Indeed, SEMs of annealed films show grains that range from 100s of nm to microns in size (Fig. 3).

Fig. 2b shows the visible photoluminescence observed while exciting the $Cs_2AgInCl_6$ films at 370 nm. A broadband emission between 400 nm to 800 nm centered at around 630 nm and matching those reported in the literature was observed for both the unannealed and annealed films.[2] The origin of this emission will be discussed below. Fig. 2c shows the excitation spectra of as-deposited and annealed $Cs_2AgInCl_6$ films while monitoring the emission at 630 nm. Like the absorbance, the emission intensity peaks at 370 nm (3.35 eV) and reaches zero at approximately 410 nm (3 eV). Thus, the excitation spectra suggest that the $Cs_2AgInCl_6$ bandgap is around 3 eV. The annealed films show higher PL at 630 nm. We attribute this to the annealing of nonradiative defects and a reduction of surfaces and grain boundary areas consistent with the grain size effect reported in the literature.[3] Indeed, annealing shows grain growth with grain sizes ranging from several hundred nm to over one micron in annealed films. Fig. 3 compares the SEM images of the as-deposited and annealed films. SEMs taken nine months later do not show any obvious visual changes (Supplementary Information Fig. S3).

We addressed the debate surrounding the origin of the emission at 630 nm by depositing $Cs_2NaBiCl_6$ (E_g = 3.1 eV), $Cs_2AgBiCl_6$ (E_g = 2.7 eV), and $Cs_2AgBiBr_6$ (E_g = 2.2 eV), in addition to $Cs_2AgInCl_6$ and measuring their PL. We hypothesized that if the orange-red emission at ~630 nm originates from self-trapped excitons, the corresponding PL from these four perovskites, with band gaps spanning ≈ 1eV (Fig. 4b), should red-shift significantly. Surprisingly, we observe (Fig. 4a) this emission at 698 nm, 656 nm, and 630 nm for $Cs_2NaBiCl_6$ (E_g = 3.1 eV), $Cs_2AgBiCl_6$ (E_g = 2.7 eV), and $Cs_2AgBiBr_6$ (E_g = 2.2 eV), respectively, shifting only 10s of nm from 630 nm for $Cs_2AgInCl_6$ and not following the band gap energy trend. For instance, with a similar E_b, E_{st}, and E_d, the PL wavelength should shift $Cs_2AgInCl_6$ to $Cs_2AgBiBr_6$ nearly 0.8 eV, from around ≈ 2 eV to ≈ 1.2 eV or by ≈ 400 nm to ≈ 1030 nm. Instead, the emission remains nearly at the same value. Concluding that this emission is due to self-trapped excitons alone would require an extremely unlikely scenario where the exciton binding (E_b), self-trapping (E_{st}), and lattice distortion (E_d) energies are shifted nearly the same amount as the differences between the band gaps of these four double perovskites to give rise to PL emission at nearly the same wavelength ($E_{PL} = E_g - E_b - E_d - E_{st}$). In fact, given the similarities in structure and octahedra, one would expect self-trapping (E_{st}), and lattice distortion (E_d) energies not to change as much as the band gap energies. Thus,

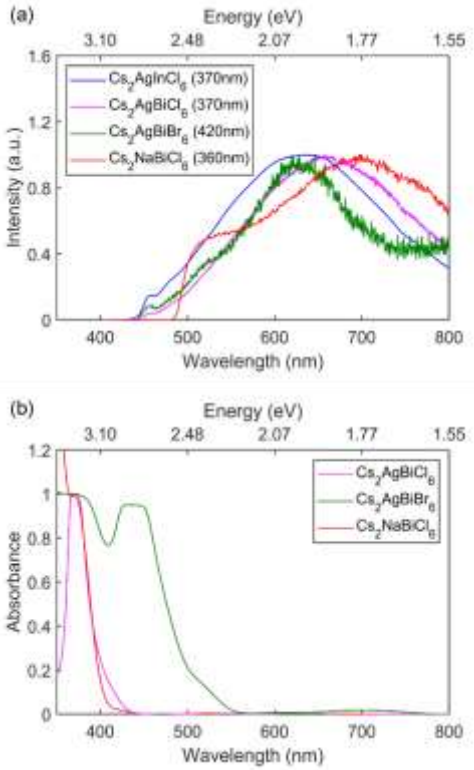

Fig. 4 (a) Emission spectra of $Cs_2AgInCl_6$, $Cs_2AgBiCl_6$, $Cs_2AgBiBr_6$, and $Cs_2NaBiBr_6$ thin films when excited at 370 nm, 370 nm, 420 nm, and 360 nm, respectively. The spectra have been normalized with the maximum value of each spectrum. Unnormalized spectra are shown in Fig. S4. (b) Optical absorbance of $Cs_2AgBiCl_6$ and $Cs_2AgBiBr_6$ thin films corrected by subtracting the interference fringes. All films were annealed at 300 °C for 1 h. Spectra in b are normalized by their maximum value between 364 nm to 399 nm.

we conclude that at least some of this emission at ≈ 2 eV observed in $Cs_2AgInCl_6$ and other double perovskites originates from a similar common defect, not only due to self-trapped excitons. Indeed, DFT calculations by Li *et al.*[35] placed Ag antisite defects In_{Ag} and Bi_{Ag} at ≈ 2 eV above the top of the valence band in $Cs_2AgInCl_6$ and $Cs_2AgBiCl_6$, respectively.

Yb-doped films

We incorporated 0-12% Yb (% of the B sites, Ag or In) into the $Cs_2AgInCl_6$ films by co-evaporating $YbCl_3$ during the deposition. Fig. 5 shows XRD from films doped with 0-12% Yb and annealed at 300 °C for one hour. At least up to 12% Yb could be incorporated without affecting the $Cs_2AgInCl_6$ crystal structure or introducing impurity phases. The (400) texturing in undoped films disappears, and the XRD patterns nearly match that of a powder diffraction pattern, indicating that the lower energy of the (400) planes responsible for the texturing in the absence of Yb is made irrelevant by Yb doping. This observation suggests that at least some of the Yb is segregating to the surfaces and equalizing the surface energies of the crystal planes such that the driving force for texturing, surface energy differences between different crystallographic planes, is eliminated. Such segregation and oxidation to form a passivating Yb_2O_3 were recently reported in $CsPbCl_3$.[36]

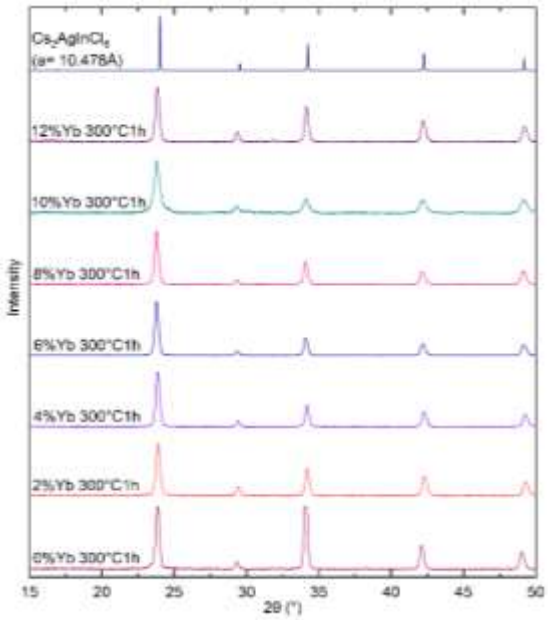

Fig. 5 XRD patterns (from the bottom up) of the $Cs_2AgInCl_6$ thin films doped with 0%, 2%, 4%, 6%, 8%, 10% and 12% Yb. All films shown were annealed at 300 °C for 1 h. All XRD patterns were measured under ambient conditions. The simulated XRD pattern of $Cs_2AgInCl_6$ with a lattice parameter a = 10.478 Å is shown for comparison.

Consistent with this, in some XRD patterns, like that of the film doped with 10% Yb in Fig. 5, we detect a very small peak at 30° which may be due to the most intense (222) peak of Yb_2O_3. The optical extinction (Fig. 6 and Fig. S5) and SEMs (Fig. S6) of Yb-doped films also support this conclusion (*vide infra*). The elemental composition of the film doped with 4% Yb and annealed at 300 °C for one hour was 23 % Cs, 10 % Ag, % In, 56.5% Cl, and 0.5% Yb, close to the expected composition of $Cs_2AgInCl_6$ (20% Cs, ~10% Ag, ~10% In, and 60% Cl and 0.4% Yb – assuming Yb substitutes in Ag or In sites) within the error of EDS.

Optical Properties of Yb-doped $Cs_2AgInCl_6$ Films

Fig. 6 compares the optical extinction of $Cs_2AgInCl_6$ films doped with 4% Yb and annealed at two different temperatures (250 °C and 300 °C) for one hour to that of an undoped film. (Wider range spectra from 350 nm to 2000 nm and spectra for all Yb doping levels are shown in the Supplementary Information as Fig. S5.) Fig. 6 shows that optical scattering is significantly reduced upon Yb doping. The absorbance baseline decreases to zero, and clear interference fringes and oscillations appear in annealed films' optical extinction spectra. This suggests that grains are much smaller in Yb-doped films than those in undoped films and do not scatter visible light efficiently. The oscillations appear due to constructive and destructive interference between light reflecting from the smooth film-air surface and the film-substrate interface. SEM images confirm this conclusion and show that grains are much smaller in annealed Yb-doped films (Fig. S6). Thus, we conclude that Yb doping inhibits grain growth by segregating to the surface, a phenomenon observed previously in $CSPbCl_3$ and $CsPbBr_3$ PVD.[28,36]

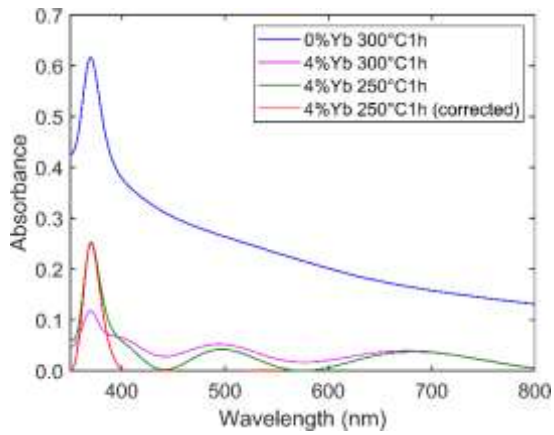

Fig. 6 Optical extinction of an undoped (0% Yb) and a $Cs_2AgInCl_6$ film doped with 4% Yb after annealing at 300 °C for one hour. Optical extinction a $Cs_2AgInCl_6$ film doped with 4% Yb after annealing at 250 °C for one hour and optical absorbance of the same film after subtracting interference fringes .

The scattering from the undoped films disappeared completely for films doped with 4% and annealed at 250 °C with interference fringes modulating fully until absorption onset around ~400 nm. We could easily correct the optical extinction by subtracting the interference fringes using a method described previously.[31] With scattering eliminated and interference corrected, we obtained a clear absorbance spectrum with onset at 400 nm (3.1 eV), within the error of the band gap (3 eV) obtained from the excitation spectra shown in Fig. 2. The effect of annealing conditions and durations on the optical absorption are shown in Fig. S7.

We measured the NIR emission from undoped and Yb-doped $Cs_2AgInCl_6$ films (all annealed at 300 °C for one hour in a nitrogen-filled glovebox) while exciting them at 370 nm. The NIR PL spectra scaled by the corresponding PLQY values (Fig. 7c) are shown in Fig. 7a. The emission shows a fine structure comprised of twelve peaks at 927 nm, 941 nm, 954 nm, 967 nm, 973 nm, 981 nm, 988 nm, 996 nm, 1006 nm, 1017 nm, 1034 nm, and 1050 nm. We attribute this structure to Stark splitting of the $^2F_{5/2}$ and $^2F_{7/2}$ energy levels of the Yb^{3+} ion by the crystal field of the host material.[37] If the Yb^{3+} ions are in a crystal field with lower than cubic symmetry, the $^2F_{5/2}$ and $^2F_{7/2}$ levels resulting from spin-orbit coupling are split in the $Cs_2AgInCl_6$ crystal field into three and four levels, respectively.[38] Twelve emission peaks are expected if all levels can be excited by energy transfer from exciton relaxation in the host. Fig. 8 shows the nonlinear least squares fitting of 12 peaks to the spectrum of the film doped with 4% Yb and a tentative energy level diagram consistent with these emissions (see also Table S1). Fig. 8b is tentative because there could be several locations where Yb can go in the $Cs_2AgInCl_6$ lattice and symmetries, and the magnitudes of crystal field splitting can be slightly different for these locations. Low-temperature NIR PL measurements are needed and are now underway to resolve this fine structure. The peak at 1080 nm appears in the absence of Yb and is assigned to a host emission instead of Yb and excluded in the calculation for PLQY.

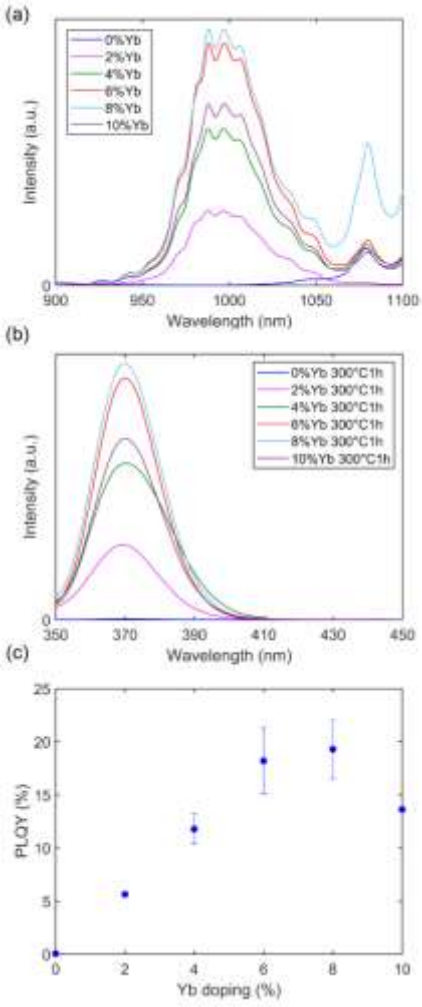

Fig. 7 (a) Yb doping variation of the NIR PL emission spectrum. The peak intensities were scaled by their corresponding PLQY measured in the integrating sphere (except the 0% Yb film). In calculating PLQY the integration of area under the curve was taken between 900 nm to 1065 nm to exclude the peak at 1080. (b) Excitation spectra of the NIR PL emission intensity at 990 nm of the films in (a). The peak intensity heights were scaled with the corresponding film's PLQY. (c) NIR PLQY of the $Cs_2AgInCl_6$ films as a function of Yb doping. The films were annealed at 300 °C for one hour in a nitrogen-filled glove box.

Fig. 7b shows the excitation spectra of the NIR emission at 990 nm scaled by the PLQY values measured in the integrating sphere. NIR emission intensity reaches its highest at 370 nm (3.3 eV), where film absorption also peaks and drops to zero at approximately 410 nm (3 eV), demonstrating the same features as the host emission and again suggesting that the band gap is approximately 3 eV.

Fig. 7c shows the NIR PLQY values as a function of Yb doping. The PLQY increases with Yb doping and reaches its highest value, ≈20% at 8% Yb, decreasing thereafter, possibly due to concentration quenching. This value is lower than that achieved in the lower band gap $Cs_2AgBiBr_6$. The orange emission at 630 nm is stronger in $Cs_2AgInCl_6$ than in $Cs_2AgBiBr_6$, possibly competing with the Yb^{3+} emission. Consistent with this competition, the intensity of the 630 nm emission is reduced in films doped with Yb (Fig. S8). Other annealing conditions were also tested on the 4% Yb doped films, including annealing at

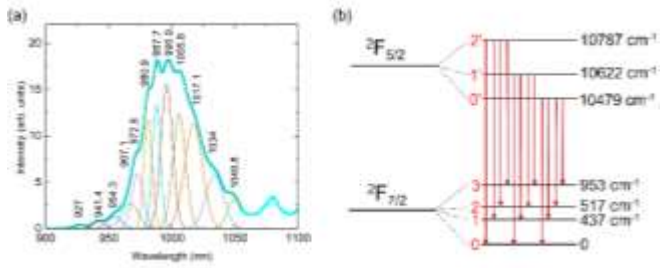

Fig. 8 (a) NIR PL emission spectrum of a $Cs_2AgInCl_6$ film doped with 4 % Yb fit with 12 Gaussian peaks. (b) Tentative crystal splitting of the $^2F_{5/2}$ and $^2F_{7/2}$ levels.

different temperatures from 250 °C to 400°C for one and two hours. The PLQY increased from ≈10% for films annealed at 250 °C to ≈15% for films annealed at 350°C. There was no detectable difference between films annealed for one or two hours except at 400 °C, where the film annealed for two hours showed lower PLQY than the film annealed for one hour (Fig. S9).

Fig. 9a shows the TRPL decay curves for select films. (See supplementary information for additional data). All TRPL curves could be fitted with the sum of three exponential functions, each with different time constants. Specifically, the orange, 630 nm PL excited at 370 nm exhibited three decay time constants, a fast decay, τ_1, varying in the 5-10 ns range, an intermediate decay, τ_2, varying in the 40-60 ns range and slow decay, τ_3, varying in the 180-240 ns range. For instance, Fig. 9a illustrates the effect of annealing temperature for an undoped film and the effect of doping for a film annealed at 350 °C for one hour. These time constants varied weakly with Yb concentration (Fig. 9b), annealing temperature, and duration (Fig. S10). Multiple time constants may indicate the heterogeneity of the trap emission or result from nonlinear recombination kinetics.[39,40] Indeed, we could fit these curves equally well with a combination of first and second-order charge carrier recombination. We use this classical multiexponential analysis only to parametrize the changes in the decay curves and, following Pean *et al.*'s[40] advice, do not interpret or ascribe any meaning to them. Surprisingly there were no significant differences in these decay time constants with Yb doping until 10% Yb doping (Fig. 9b). At 10% Yb doping, the intermediate and fast time constants decreased significantly, coinciding with the NIR PLQY decrease (Fig. 7). This is consistent with increased nonradiative recombination perhaps via concentration quenching. Approximate calculations suggest that concentration quenching for homogeneously distributed Yb should become important above approximately 2% doping, much less than 10%, but Yb distribution may not be uniform with possible Yb segregation to grain boundaries and surfaces. That NIR PLQY increases with little change in the lifetimes of the orange emission between 0-8% Yb doping suggests that the two do not compete with each other but rather with a third nonradiative decay channel.

We also tested the temporal stability of the PLQY and the robustness of the PLQY measurements with subtle changes in

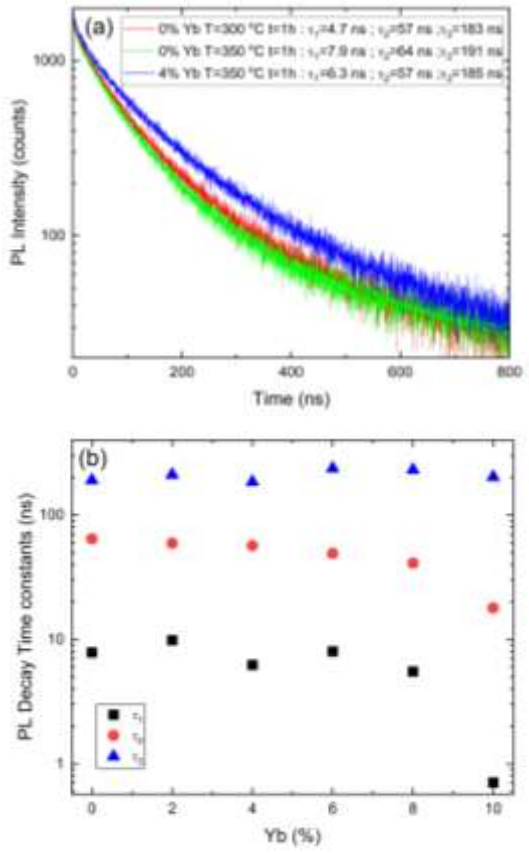

Fig. 9 (a) TRPL decay curves for undoped and Yb-doped $Cs_2AgInCl_6$ films. Solid lines are triexponential fit to the data with time constants in the legend. (b) TRPL decay time constants as a function of Yb concentration for $Cs_2AgInCl_6$ films annealed at 350 °C for 1 h.

the annealing protocol for a film doped with 4% Yb and annealed at 300 °C for one hour. Specifically, we compared the PLQY from films cooled naturally to room temperature on the hot plate after turning off the hot plate ("slow cooling"), cooled by taking them off the hot plate and placing them on a room temperature surface ("quenched") and annealing in the air at the same temperature and duration (air-annealed). While there is scatter in the measurements, no significant difference was observed in PLQY. The average PLQY of all the above measurements was 11.8%, with a standard deviation of 1.4% (Fig. S11). The film PLQY remained in a range of around ≈12% after exposure to air for nearly a month.

Conclusions

We deposited $Cs_2AgInCl_6$ double perovskite films by co-evaporating CsCl, AgCl, and $InCl_3$ in a PVD system. $Cs_2AgInCl_6$ is stable at room temperature and forms upon deposition and reaction of the precursors on the substrate, even at temperatures as low as 30 °C. Small amounts of impurity phase $Cs_3In_2Cl_9$ and unreacted precursor AgCl are detected in the as-deposited film but disappear when the films are annealed at 300 °C or 350 °C. Undoped $Cs_2AgInCl_6$ exhibits a broadband

emission peaking at 630 nm. This same emission is observed, albeit at different intensities, from other double perovskites, including $Cs_2AgBiCl_6$, $Cs_2AgBiBr_6$, and $Cs_2NaBiCl_6$, suggesting that it originates from similar defects in these materials. $Cs_2AgInCl_6$ bandgap is determined to be 3 eV, and absorption peaks at 370 nm. Up to 12% Yb could be incorporated into the film without changing the cubic structure of $Cs_2AgInCl_6$. Yb-doped films excited at 370 nm show NIR emission corresponding to transitions between the $^2F_{5/2}$ and $^2F_{7/2}$ energy levels of the Yb^{3+} ion. The fine structure of this emission shows that the $^2F_{5/2}$ and $^2F_{7/2}$ levels are split in the $Cs_2AgInCl_6$ crystal field. The NIR PLQY increases with increasing Yb concentration; the highest value is reached at 8% Yb.

Author Contributions

YL and ESA conceptualized the study, decided on the methodology, and conducted the investigation and formal analysis. All authors contributed to data collection and curation (YL, IJC, SS for $Cs_2AgInCl_6$, PJ for $Cs_2AgBiCl_6$, and MT for $Cs_2AgBiBr_6$ and $Cs_2NaBiCl_6$, KS, and RSR contributed partially to all materials.) YL wrote the original draft, and ESA edited all versions; all other authors read and reviewed the final version and provided final edits.

Conflicts of interest

MN, IJC, ESA, and New York University (NYU) have filed a patent on Yb-doped double perovskites $Cs_2AgBi(Cl,Br)_6$ for use as downconversion materials on silicon solar cells.

Acknowledgments

The research used the New York University (NYU) Shared Instrumentation facility's X-ray diffraction and electron microscopy equipment. NYU's X-ray diffraction facility was supported by the Materials Research Science and Engineering Center (MRSEC) program of the National Science Foundation under Award Numbers DMR-082034 and DMR-1420073 by the National Science Foundation. MERLIN (Carl Zeiss) field emission scanning electron microscope (FESEM) instrument was purchased with financial support from the MRI program of the National Science Foundation under Award DMR-0923251. E.S.A. gratefully acknowledges support from Alstadt Lord Mark Chair.

References

1 G. Volonakis, A. A. Haghighirad, R. L. Milot, W. H. Sio, M. R. Filip, B. Wenger, M. B. Johnston, L. M. Herz, H. J. Snaith and F. Giustino, *J. Phys. Chem. Lett.*, 2017, **8**, 772–778.

2 J. Luo, X. Wang, S. Li, J. Liu, Y. Guo, G. Niu, L. Yao, Y. Fu, L. Gao, Q. Dong, C. Zhao, M. Leng, F. Ma, W. Liang, L. Wang, S. Jin, J. Han, L. Zhang, J. Etheridge, J. Wang, Y. Yan, E. H. Sargent and J. Tang, *Nature*, 2018, **563**, 541–545.

3 P. Han, X. Zhang, X. Mao, B. Yang, S. Yang, Z. Feng, D. Wei, W. Deng, T. Pullerits and K. Han, *Sci. China Chem.*, 2019, **62**, 1405–1413.

4 T. T. Tran, J. R. Panella, J. R. Chamorro, J. R. Morey and T. M. McQueen, *Mater. Horizons*, 2017, **4**, 688–693.

5 J. Zhou, Z. Xia, M. S. Molokeev, X. Zhang, D. Peng and Q. Liu, *J. Mater. Chem. A*, 2017, **5**, 15031–15037.

6 N. N. K. and A. Nag, *Chem. Commun.*, 2018, **54**, 5205–5208.

7 F. Locardi, M. Cirignano, D. Baranov, Z. Dang, M. Prato, F. Drago, M. Ferretti, V. Pinchetti, M. Fanciulli, S. Brovelli, L. De Trizio and L. Manna, *J. Am. Chem. Soc.*, 2018, **140**, 12989–12995.

8 J. Luo, S. Li, H. Wu, Y. Zhou, Y. Li, J. Liu, J. Li, K. Li, F. Yi, G. Niu and J. Tang, *ACS Photonics*, 2018, **5**, 398–405.

9 Z. Xiao, K. Du, W. Meng, D. B. Mitzi and Y. Yan, *Angew. Chemie*, 2017, **129**, 12275–12279.

10 A. Jain, O. Voznyy and E. H. H. Sargent, *J. Phys. Chem. C*, 2017, **121**, 7183–7187.

11 T. Zhang, Z. Cai and S. Chen, *ACS Appl. Mater. Interfaces*, 2020, **12**, 20680–20690.

12 F. Zhao, Z. Song, J. Zhao and Q. Liu, *Inorg. Chem. Front.*, 2019, **6**, 3621–3628.

13 W. Meng, X. Wang, Z. Xiao, J. Wang, D. B. Mitzi and Y. Yan, *J. Phys. Chem. Lett.*, 2017, **8**, 2999–3007.

14 B. Yang, X. Mao, F. Hong, W. Meng, Y. Tang, X. Xia, S. Yang, W. Deng and K. Han, *J. Am. Chem. Soc.*, 2018, **140**, 17001–17006.

15 S. Li, Z. Shi, F. Zhang, L. Wang, Z. Ma, D. Wu, D. Yang, X. Chen, Y. Tian, Y. Zhang, C. Shan and X. Li, *ACS Appl. Mater. Interfaces*, 2020, **12**, 46330–46339.

16 Q. Liao, J. Chen, L. Zhou, T. Wei, L. Zhang, D. Chen, F. Huang, Q. Pang and J. Z. Zhang, *J. Phys. Chem. Lett.*, 2020, **11**, 8392–8398.

17 C. Wang, P. Liang, R. Xie, Y. Yao, P. Liu, Y. Yang, J. Hu, L. Shao, X. Sun, F. Kang and G. Wei, *Chem. Mater.*, 2020, **32**, 7814–7821.

18 F. Locardi, E. Sartori, J. Buha, J. Zito, M. Prato, V. Pinchetti, M. L. Zaffalon, M. Ferretti, S. Brovelli, I. Infante, L. De Trizio and L. Manna, *ACS Energy Lett.*, 2019, **4**, 1976–1982.

19 S. M. Ferro, M. Wobben and B. Ehrler, *Mater. Horizons*, 2021, **8**, 1072–1083.

20 Y. Liu, A. Nag, L. Manna and Z. Xia, *Angew. Chemie*, 2021, **133**, 11696–11707.

21 W. Lee, S. Hong and S. Kim, *J. Phys. Chem. C*, 2019, **123**, 2665–2672.

22 Y. Mahor, W. J. Mir and A. Nag, *J. Phys. Chem. C*, 2019, **123**, 15787–15793.

23 L. Cao, X. Jia, W. Gan, C. Ma, J. Zhang, B. Lou and J. Wang, *Adv. Funct. Mater.*, 2023, **33**, 2212135.

24 D. Chen, X. Zhang, J. Wei, L. Zhou, P. Chen, Q. Pang and J. Z. Zhang, *Inorg. Chem. Front.*, 2022, **9**, 4695–4704.

25 H. Arfin, J. Kaur, T. Sheikh, S. Chakraborty and A. Nag, *Angew. Chemie Int. Ed.*, 2020, **59**, 11307–11311.

26 Z. Rao, Q. Li, Z. Li, L. Zhou, X. Zhao and X. Gong, *J. Phys. Chem. Lett.*, 2022, **13**, 3623–3630.

27 S. Jin, R. Li, H. Huang, N. Jiang, J. Lin, S. Wang, Y. Zheng, X. Chen and D. Chen, *Light Sci. Appl.*, 2022, **11**, 52.

28 I. J. Cleveland, M. N. Tran, A. Dey and E. S. Aydil, *J. Vac. Sci. Technol. A Vacuum, Surfaces, Film.*, , DOI:10.1116/6.0000875.

29 M. N. Tran, I. J. Cleveland and E. S. Aydil, *ACS Appl. Electron. Mater.*, 2022, **4**, 4588–4594.

30 M. N. Tran, I. J. Cleveland, J. R. Geniesse and E. S. Aydil, *Mater.*

Horizons, 2022, **9**, 2191–2197.
31 Y. Liu, I. J. Cleveland, M. N. Tran and E. S. Aydil, *J. Phys. Chem. Lett.*, 2023, **14**, 3000–3006.
32 Y. Liu, M. N. Tran, I. J. Cleveland and E. S. Aydil, *J. Vac. Sci. Technol. B*, 2023, **41**, 022206.
33 R. Swanepoel, *J. Phys. E.*, 1983, **16**, 1214–1222.
34 K. Momma and F. Izumi, *J. Appl. Crystallogr.*, 2011, **44**, 1272–1276.
35 T. Li, X. Zhao, D. Yang, M.-H. Du and L. Zhang, *Phys. Rev. Appl.*, 2018, **10**, 041001.
36 I. J. Cleveland, M. N. Tran, S. Kabra, K. Sandrakumar, H. Kannan, A. Sahu and E. S. Aydil, *Phys. Rev. Mater.*, 2023, **7**, 065404.
37 S. Dai, A. Sugiyama, L. Hu, Z. Liu, G. Huang and Z. Jiang, *J. Non. Cryst. Solids*, 2002, **311**, 138–144.
38 J. Y. D. Roh, M. D. Smith, M. J. Crane, D. Biner, T. J. Milstein, K. W. Krämer and D. R. Gamelin, *Phys. Rev. Mater.*, 2020, **4**, 105405.
39 L. Santamaria, P. Maddalena and S. Lettieri, *Materials (Basel).*, 2022, **15**, 1515.
40 E. V. Péan, S. Dimitrov, C. S. De Castro and M. L. Davies, *Phys. Chem. Chem. Phys.*, 2020, **22**, 28345–28358.